




The near-infrared polarization of the pre-planetary nebula Frosty Leo

E. O. Serrano Bernal ¹★, L. Sabin ², A. Luna,¹ R. Devaraj ^{1,3}, Y. D. Mayya¹
and L. Carrasco¹

¹*Instituto Nacional de Astrofísica, Óptica y Electrónica, C.P. 72840, San Andrés Cholula, Puebla, Mexico*

²*Instituto de Astronomía, Universidad Nacional Autónoma de México, Apdo. Postal 877, 22860 Ensenada, B. C., Mexico*

³*Dublin Institute for Advanced Studies, Astronomy and Astrophysics Section, 31 Fitzwilliam Place, Dublin 2, Ireland*

Accepted 2020 April 28. Received 2020 April 28; in original form 2019 July 12

ABSTRACT

We present a near-infrared imaging polarimetric study of the pre-planetary nebula: Frosty Leo. The observations were carried out in J , H , and K' bands using the new polarimeter POLICAN mounted on the 2.1-m telescope of the Guillermo Haro Astrophysical Observatory, Sonora, Mexico. The most prominent result observed in the polarization maps is a large and well-defined dusty envelope (35 arcsec diameter in H band). The polarization position angles in the envelope are particularly well ordered and nearly parallel to the equator of the nebula (seen in J and H bands). The nebula presents a known bipolar outflow and the envelope completely wraps around it. Within the bipolar lobes, we find high polarization levels ranging from 60 per cent (J band) to 90 per cent (K' band) and the polarization angles trace a centrosymmetric pattern. We found the remnants of superwind shells at the edges of the bipolar lobes and the duration of this phase is around 600 yr. The origin of polarization features in the nebula is most likely due to a combination of single and multiple scattering. Our results clearly demonstrate new structures that provide new hints on the evolution of Frosty Leo from its previous asymptotic giant branch phase.

Key words: polarization – scattering – stars: AGB and post-AGB – infrared: general.

1 INTRODUCTION

Pre-planetary nebulae (PPNe) are evolved low–intermediate-mass stars in a transitional stage between the asymptotic giant branch (AGB) and planetary nebula phases (Kwok 1993). PPNe display a circumstellar envelope (CSE) of dust and gas which was formed as a result of the mass loss (up to $10^{-5} M_{\odot} \text{ yr}^{-1}$, Loup et al. 1993) suffered during their previous AGB phase. The CSEs keep records of the mass-loss history and in consequence, their study can help to understand their, often, intriguing morphology.

PPNe are mostly seen by scattered light in the optical and near-infrared (NIR), so, they are expected to be linearly polarized. Taking advantage of this, Gledhill et al. (2001) and Gledhill (2005) performed NIR imaging polarimetry not only to detect the faint CSEs from several PPNe, but also to resolve structures within them. Thus, polarimetry is a useful tool to study the CSE of PPNe.

In this work, we present the results of the polarimetric observations of the well-known PPN Frosty Leo (IRAS 09371+1212). It was first identified as a post-AGB with a bipolar structure by Forveille et al. (1987). Later, NIR images and spectroscopic observations confirmed its morphology and the presence of ice

water (Hodapp, Sellgren & Nagata 1988). By assuming that the central star has a spectral type K7III or II, Mauron, Le Borgne & Picquette (1989) estimated a distance between 1.7 and 4.3 kpc, and the stellar temperature which corresponds to the spectral type is 3750 K (Robinson, Smith & Hyland 1992).

Several works investigated this intriguing object and due to its dusty nature, polarimetry appeared as a useful tool. By means of imaging polarimetry, Clemens & Leach (1987) unveiled an extended but irregular polarized envelope at visible wavelengths. In the NIR, polarimetric studies of Frosty Leo have focused on its central region. The first analysis was performed by Dougados et al. (1990) using the 3.6-m CFH telescope and the CIRCUS IR camera. Within a small region of 8 arcsec \times 8 arcsec, they detected a centrosymmetric polarization pattern as well as the signature of an edge-on warped dust disc. Later on, Murakawa et al. (2008) used the 8-m Subaru telescope equipped with a coronagraph and adaptive optics to observe the central part of Frosty Leo within a 10 arcsec \times 10 arcsec area. They reported some new polarimetric features such as an almost straight depolarized region and a slight vector alignment in a small spot on the equator.

High-resolution imaging polarimetry has allowed a better understanding of Frosty Leo's central part. However, a lot can still be learned from this object at a larger scale. Indeed, a bigger field of view (FoV) is desirable when it comes to the study of the outer

* E-mail: arthas1900@hotmail.com

Table 1. NIR magnitudes (2MASS) of Frosty Leo and integration time for each band.

POLICAN IR band	2MASS magnitude	t_{int} (s)
J (1.24 μm)	8.06	1200
H (1.63 μm)	7.48	1200
K' (2.12 μm)	7.46 (K)	2400

structure. For this object, imaging polarimetry was performed with the NIR polarimeter of Cananea, POLICAN (Devaraj et al. 2018a). The combination of a large FoV and an instrument with good sensitivity, even with a 2-m telescope, can lead to some new findings as it will be presented in the sections ahead. The structure of the paper is as follows: we describe the observations and data reduction in Section 2, in Section 3 we present our results, discussion of the observed polarization will be carried on in Section 4, and our concluding remarks are shown in Section 5.

2 OBSERVATIONS AND DATA REDUCTION

Imaging polarimetry of Frosty Leo was performed at the 2.1-m Guillermo Haro Astrophysical Observatory (OAGH) telescope, at Sonora, Mexico, using POLICAN mounted on the Cananea near-infrared camera (CANICA, Carrasco et al. 2017). The 1024×1024 element HgCdTe detector is sensitive between 0.85 and 2.4 μm , and was used in conjunction with J (1.24 μm), H (1.63 μm), and K' (2.12 μm) broad-band filters. The 2:1 focal reducer of CANICA provides a scale plate of $0.32 \text{ arcsec pixel}^{-1}$ and the FoV of around 5 arcmin.

The single-beam polarimetric module of (POLICAN) consists of a rotating half-wave plate (HWP) and a wire grid linear polarizer placed in front of CANICA. Both elements are placed near the focal plane and their diameters allow to use the full 5 arcmin FoV. In order to measure the linear polarization, the HWP is rotated to 4 position angles (0° , 45° , 22.5° , and 67.5°) to complete one set of four images. Several sets of dithered images are obtained to calculate and subtract the sky emission to later compute the Stokes parameters. Major insight of POLICAN's features and the standard observing methods are described in detail by Devaraj et al. (2018a).

The observations were carried out during two runs. The first took place during 2017 April 14 and 15 and the second one was carried out during the nights of 2018 February 23–25. Weather conditions were good for both runs and the seeing was about 1 arcsec. For J and H bands, we used the standard ‘dithering scheme’, in which 10 dithered sets of images were obtained with exposure time of 30 s per frame. This results in a total integration time of 1200 s. For K' band, we followed a similar scheme, although, to avoid background saturation and boost signal-to-noise ratio, the images were co-added three times with a exposure time of 20 s. The total integration time in K' band was 2400 s (see Table 1).

Data reduction for POLICAN consists of three steps: first, standard corrections as flat fielding, dark current, and background subtraction are performed. Later, the images are stacked and aligned to a common coordinate system, several IRAF packages were used to develop such routines. In the second step, the Stokes parameters Q and U are calculated and later corrected to eliminate any instrumental polarization, such as the HWP offset angle, θ_{off} , and the intrinsic degree of polarization P_{inst} . Finally, the polarization angle, $\text{PA} = 0.5 \times \tan^{-1}(U/Q)$, polarization degree, P per cent = $100 \sqrt{U^2 + Q^2}$, total intensity I , and error maps are

computed using PYTHON software packages. All maps presented here have a binning of 3×3 pixels to match the 1 arcsec seeing. The maximum errors in P per cent and PA are 12 per cent and 10° , respectively. The NIR magnitudes from the 2MASS catalogue (Skrutskie et al. 2006) and the integration times are shown in Table 1.

3 RESULTS

Figs 1–3 show the J , H , and K' bands polarization maps for Frosty Leo, respectively. In all three figures, the intensity (I Stokes) and polarization degree (P per cent) are shown with vectors superimposed. The vectors are parallel to the electric field E and their length is proportional to the degree of linear polarization, a reference scale vector is also shown in each map.

We emphasize that the maps in Figs 1 and 2 display a noticeable sinking to decrease in intensity in the eastern region. This might be misinterpreted as a waist-like feature, but it is an instrumental artefact caused by crosstalk between pixels during readout. Our reduction pipeline is able to remove this undesirable effect to some degree but not completely Devaraj et al. (2018b). Nevertheless, the data presented here are still reliable.

3.1 Polarization in J band

The intensity emission (Fig. 1, left-hand panel) reaches its peak at the central star location and then it decreases almost evenly in all directions, except at tips of the bipolar lobes, where a small increase is detected.

The NIR polarization in Frosty Leo was previously studied and reported by Dougados et al. (1990) in J band, although their research was only focused within a radius of 5 arcsec. They found P per cent as high as 40 per cent in the lobes close to the central star and a low polarized region across the equator. Our polarization map is in good agreement for the zones in common and extend this study to three times more radius.

The first noticeable feature in our maps is the extended envelope (EE) that protrudes from the well-known bipolar lobes of this object. Part of the EE is also seen at visible wavelengths, Clemens & Leach (1987) detected it also employing imaging polarimetry. However, our new POLICAN data reveal a larger size. To our knowledge, it is the *first detection* of this extended feature in the NIR. Since this object is fainter in the J band, the shape of the EE looks elliptical at this wavelength. However, based on our data from the H band we conclude that the actual shape is more likely spherical (see Fig. 2). We did not see any variation of the P per cent within the EE and we estimated an average of 16 per cent. The polarization vectors related to this EE show a clear east-west alignment, and the average PA of these vectors is $79^\circ \pm 10^\circ$.

Within the bipolar outflows, the polarization vectors follow a centrosymmetric pattern. Such vector behaviour suggests single scattering as the polarizing mechanism and that the optical depth in the media is low (Gledhill et al. 2001; Gledhill 2005). Previous observations at visible wavelengths obtained similar results (Scarrott & Scarrott 1994). Within a radius of 7 arcsec, we resolved three clumps (two northwards and one southwards from equator), these structures are characterized by their P per cent which are between 30 per cent and 40 per cent. A narrow and relatively low polarized area is seen between the north clumps. It could be identified with the elongated region found by Murakawa et al. (2008) in H and K bands. The authors attributed the low polarization level to a low dust density, which is in good agreement with our interpretation. Another two clumps are found at the tips of the bipolar jets and

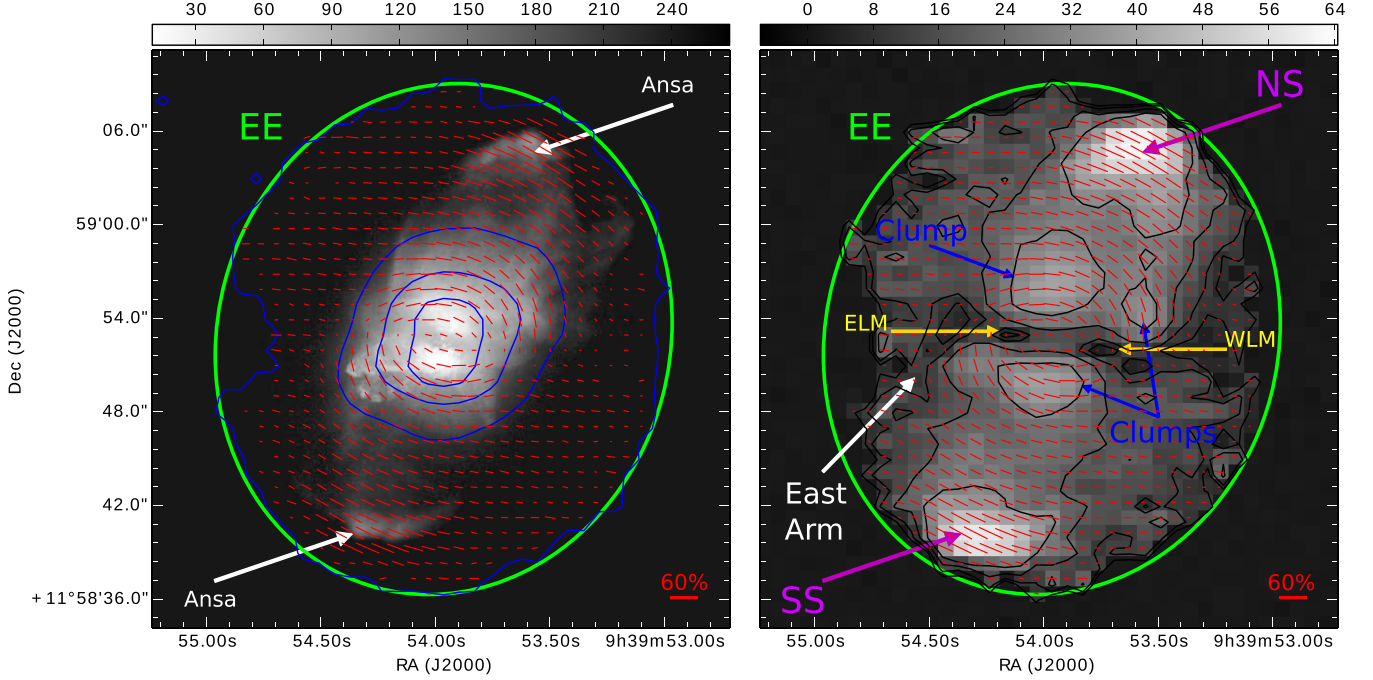


Figure 1. Polarization maps of Frosty Leo in *J* band. The left-hand panel shows an *Hubble Space Telescope* composite image (F606W and F814W filters) of Frosty Leo superimposed with (red) electric vectors. The total intensity is displayed every 2 mag in blue contour levels (arbitrary units). The right-hand panel shows the degree of polarization (P per cent) as grey-scale image. Selected contour levels (8 per cent, 17 per cent, 20 per cent, and 30 per cent) are displayed to highlight the structures unveiled by our data. The regions of interest are labelled according to the text. In both panels, an ellipse of $33 \text{ arcsec} \times 29 \text{ arcsec}$ is displayed to indicate size and geometry of the EE and the scale is shown at the top.

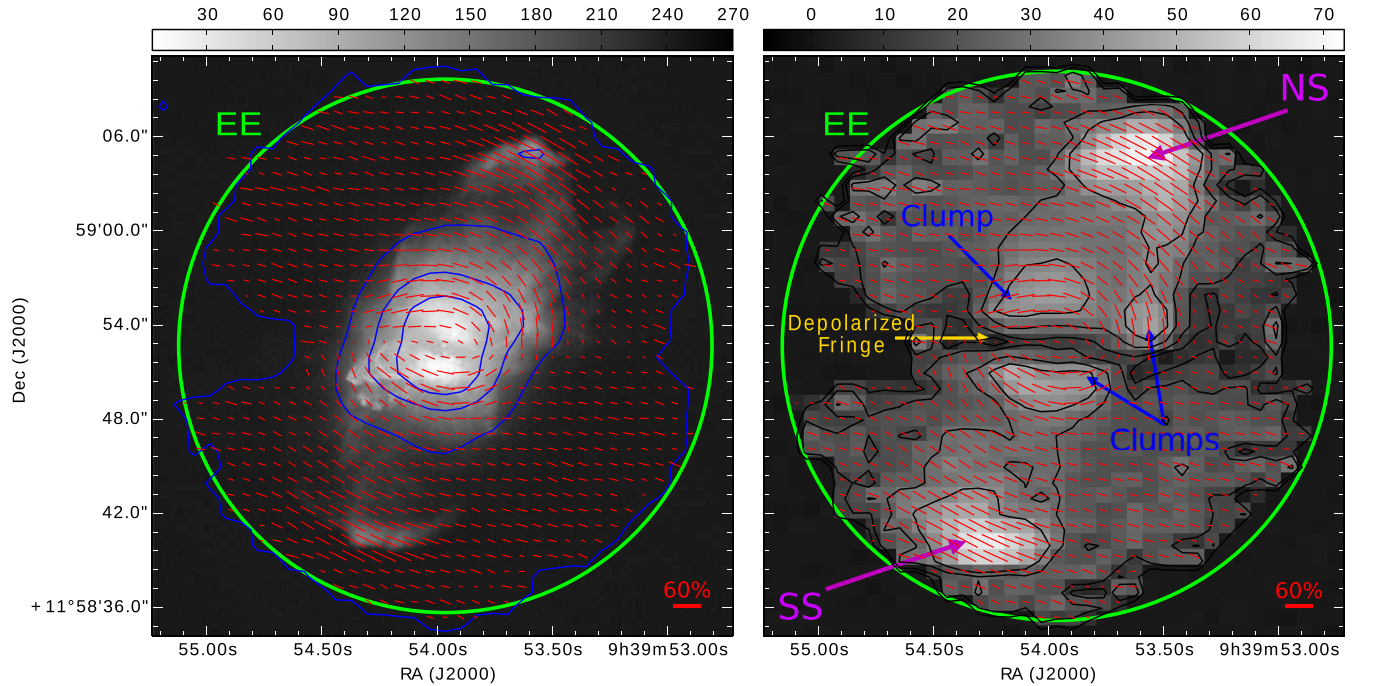


Figure 2. Polarization maps of Frosty Leo in *H* band. Details are as for Fig. 1. Contour levels in the right-hand panel correspond to 16 per cent, 26 per cent, and 36 per cent of polarization. The circle in both panels has a diameter of 35 arcsec .

because of their appearance, we labelled them NS and SS as in north and south shells, respectively. They seem to match the location of the ansae remarked by Sahai, Bujarrabal & Zijlstra (2000) and their P per cent ranges between 40 per cent and 62 per cent.

Along the equator, there is a narrow region of low polarization, often associated with a disc (Rounan et al. 1988; Hodapp et al. 1988; Dougados et al. 1990; Murakawa et al. 2008). Some of the vectors in this region are aligned and parallel to the equator, these

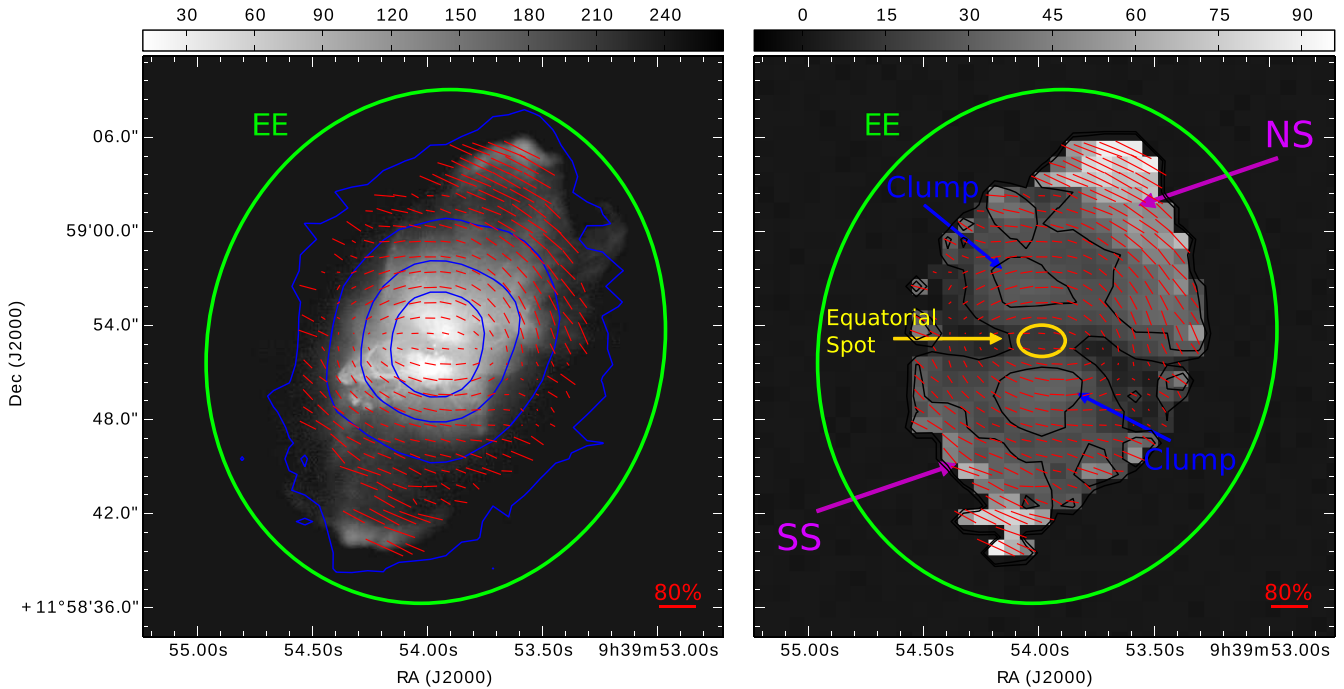


Figure 3. Polarization maps of Frosty Leo in K' band. Details are as for Fig. 1. The contour levels in the right-hand panel correspond to 13 per cent and 25 per cent of polarization. In both panels, an ellipse of $33 \text{ arcsec} \times 29 \text{ arcsec}$ is displayed for comparison.

vectors are localized between two spots of almost zero polarization: the east local minima and the west local minima (see Fig. 1, right-hand panel). Murakawa et al. (2008) found similar results in H and K bands and also suggested the dichroic mechanism as a possible explanation. A dichroic interpretation would indicate the presence of non-spherical grains with their longer axes preferentially aligned. The electric vector in the transmitted beam is thus perpendicular to that preferential direction (Lazarian 2003, 2007; Whittet 2004; Crutcher 2012).

On the eastern edge of the equator, we notice an ‘arm-like’ region of 7 arcsec length that is highlighted by its low polarization (11 per cent) and is directed towards the south. A low polarization trend is also seen towards the north-west, but it looks more diffuse and rapidly reaches our detection limit. Sahai et al. (2000) labelled a structure as north-west lobe in that same direction.

3.2 Polarization in H band

The polarization maps in H band are shown in Fig. 2. The total intensity of Frosty Leo in H band follows a trend quite similar to that in J band. Except for the low polarized arm-like area and the equatorial local minima, the polarization in H band looks quite similar to that in the previous section. We emphasize that polarization features such as the EE and the north and south shells are first time detections in the NIR.

Although our resolution is only 1 arcsec, our results are in good agreement with those shown by Murakawa et al. (2008, adaptive optics PSF, point spread function of $0.16 \text{ arcsec} \times 0.28 \text{ arcsec}$ in K band). Within a radius of 7 arcsec, the P per cent reaches between 40 per cent and 50 per cent in the clumps nearby the central star, and a depolarized fringe along the equator shows an average of 11 per cent. As in J band, some vectors in this fringe are parallel to those in the EE. This depolarized region seems to extend

Table 2. Summary results of the polarization in Frosty Leo for regions. The labels in the column of position angles are C and A for centrosymmetric and aligned, respectively.

Nebula's region	J (P per cent)	H (P per cent)	K' (P per cent)	Position angles ($^\circ$)	Polarizing mechanism
Bipolar lobes (max)	62	70	89	C	Single scattering
Extended envelope (avg)	16	20	–	A	Multiple scattering
Equatorial spot (avg)	16	11	15	A	Dichroism?

towards the east and west almost as if splitting the whole nebula in half.

Although slightly distorted by the eastern depression, the EE in H band seems mostly spherical and considerably larger than in the J -band image. Such difference in size is probably a matter of detection limit since Frosty Leo is brighter in H band by almost 1 mag (see Table 1). The diameter of the EE is of 35 arcsec and the vectors linked to this area are clearly aligned on east-west direction. We measured an average PA is $74^\circ \pm 10^\circ$ and the P per cent has a mean value of 20 per cent, which is slightly larger than in J band (see Table 2).

Along the major axis, the vectors follow a centrosymmetric pattern and the NS and SS are clearly seen in polarized light. The P per cent ranges from 36 per cent to 70 per cent and their appearance is more spread out than in J band. The NS seems to smear down southwards, almost reaching the internal clumps.

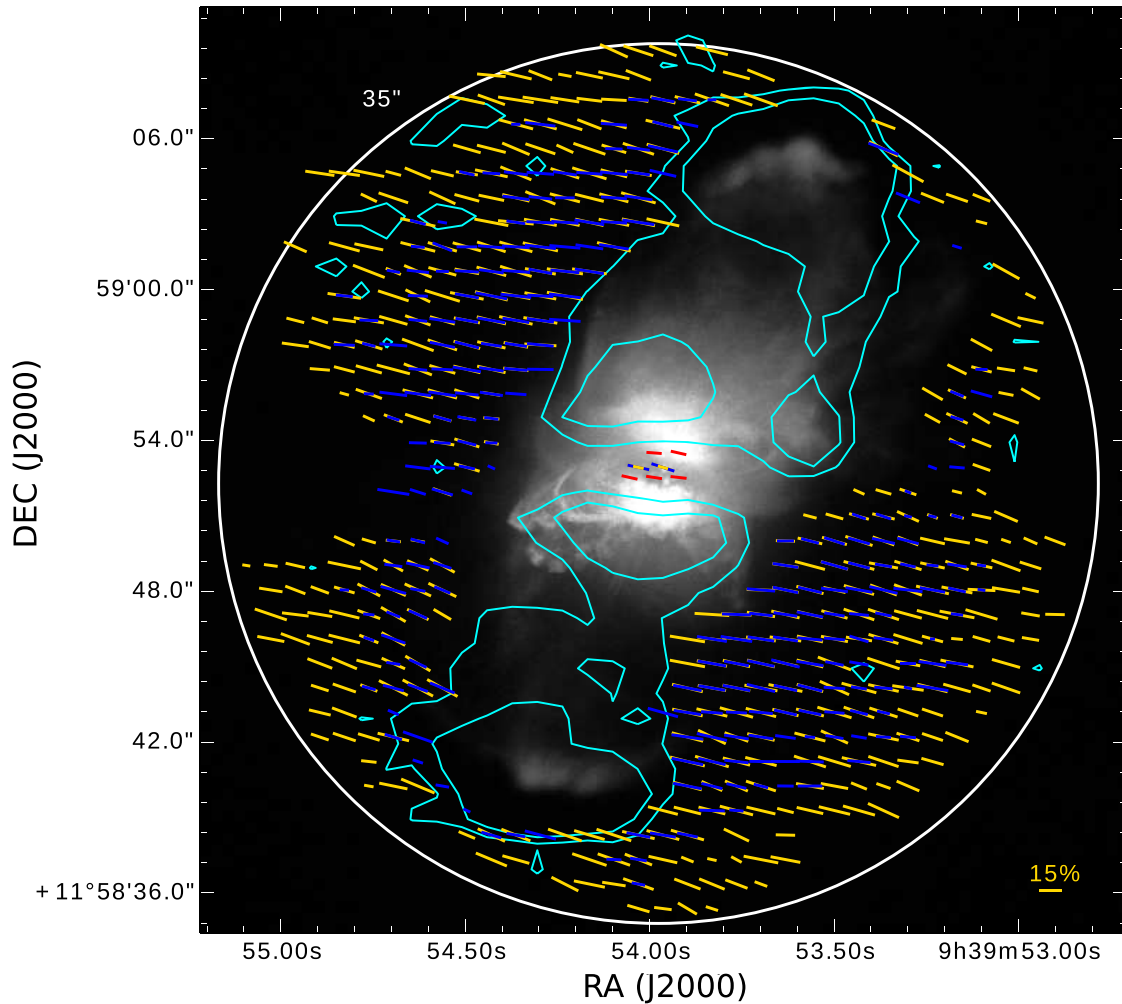


Figure 4. *Hubble Space Telescope* composite images (F606W and F814W filters) of Frosty Leo superimposed with polarization vectors. Polarization in the *J* (blue), *H* (yellow), and *K'* (red) bands are displayed. The vectors that follow a centrosymmetric pattern have been removed in all three bands. Green contour levels correspond to polarization in *H* band (same as in Fig. 2) and are displayed to remark the inner clumps and the north and south shells. The white circle delineates the EE which has a diameter of 35 arcsec in *H* band. Similar PAs are observed between bands in both, the extended emission and the ES.

3.3 Polarization in *K'* band

K'-band polarization map of Frosty Leo is shown in Fig. 3. This is (to our knowledge) the first polarization map presented in this band for this object. Given our detection limit, the EE is not seen in this map and only the bipolar nebula was clearly detected. Nevertheless, it still provide some new information on this object. As expected, most of the vectors in the map follow a centrosymmetric pattern. The exception is a small equatorial spot (ES) where several vectors are perpendicular to the nebula's axis. Although not entirely, the ES seems to match the location of some aligned vectors in the *J* and *H* images, this is better seen in Fig. 4. The vectors in the ES show an almost constant position angle of 80° , whilst the average degree of polarization is 15 per cent.

The polarized structure in this band only shows two clumps near the equator. The 'missing clump' seems to be merged with the NS. This could be an effect of poor resolution since the PSF in this band is degraded to ~ 1.5 arcsec. The polarization in the central clumps range from 25 per cent to 35 per cent.

As in the previous maps, the highest *P* per cent levels are found in the NS and SS, in some points even reaching or exceeding the

80 per cent. These high *P* per cent levels are not uncommon since other PPNe such as OH 231.8+4.2 shows similar levels and this is in agreement with a scattering process (Ageorges & Walsh 2000). The NS looks more extended and is also smearing southwards even more evidently than in *H* band. The SS is less evident given the limits of our map. Nevertheless, a large amount of material is seen at the edge of the southern side of the map and it could still be associated to the SS.

4 DISCUSSION

4.1 The polarization in the NS and SS of Frosty Leo

AGB stars produce a CSE through a slow and tenuous wind (Kwok 1993), the moderate rate of mass ejection through the AGB wind is about $10^{-5} M_\odot \text{ yr}^{-1}$ (Loup et al. 1993). At the end of the AGB lifetime, the mass-loss rate and the velocity of the expelled material increase drastically (up to $\sim 10^{-4} M_\odot \text{ yr}^{-1}$, e.g. Bujarrabal 1999; Bujarrabal et al. 2001). This period of accelerated mass loss is expected to last a few thousand years (Kaufl, Renzini & Stanghellini 1993) and is known as the superwind phase.

The global shaping of the nebula must occur at this stage of increased mass loss (Lagadec 2016). A noteworthy feature seen in many nebulae are the ansae. Ansaes are double knot-like structures along the nebula's axis (Aller 1941). These knots move in opposite directions and often, their speed is faster than the previously AGB ejected material (e.g. Patriarchi & Perinotto 1991; Redman et al. 2000; Sahai & Patel 2015). The mechanism that leads to ansae formation is still unclear, but, since they are oriented along the major axis, it is probable that they are the remnants of outflow collimation. The most likely sources of collimation are the mass transfer between a binary system (e.g. Soker & Rappaport 2000; Jones & Boffin 2017), or a magnetic field (also driven by a binary companion, Nordhaus & Blackman 2006; Nordhaus, Blackman & Frank 2007). Once collimation has taken place, ansae could be formed by diverse mechanisms (see Balick & Frank 2002 for a discussion of ansae formation).

Although their origin is not fully understood, ansae (or shells) can be used to constrain the superwind time t_{sw} (Gledhill et al. 2001). The outer and inner edges of a shell should indicate the beginning and cessation of mass loss. Thus, by using the shell's angular size and assuming expansion velocities from molecular line measurements, we can estimate the superwind time (Meixner et al. 1997; Gledhill et al. 2001).

The bipolar regions within the nebula are optically thin (centrosymmetric pattern), thus, the NS and SS are physical structures illuminated by a central source (Wolstencroft et al. 1986; Dougados et al. 1990; Gledhill et al. 2001). Since these shells are symmetric, detached from the central region and spatially correlated with ansae (see Fig. 4), we are assuming that they are the remains of a superwind event.

Our polarization maps show that the NS and SS cover an area of 51 and 42 arcsec², respectively. By inspection of the *J*-band map, where the resolution is better, the average angular size of the shells (along the polar axis) was found to be 8 arcsec. At a distance of 3 kpc (Mauron et al. 1989; Robinson et al. 1992), their length would be of ~ 0.1 pc. To estimate the superwind time t_{sw} , we used the CO speed component of 50 km s⁻¹ measured by Sahai et al. (2000) and an inclination angle of 15° (Roddiier et al. 1995):

$$t_{\text{sw}} \simeq \frac{l_{\text{sh}}}{V_{\text{exp}}} \simeq \frac{(3 \text{ kpc}) \tan(8 \text{ arcsec})}{(50 \text{ km s}^{-1}) / (\sin 15^\circ)} \simeq 600 \text{ yr.}$$

where, l_{sh} is the length of the shell and V_{exp} is the projected expansion velocity of the CO along the axis. Given the assumption of a constant speed when it actually may vary with time, this estimation should be considered as a lower limit. The computed error is 200 yr and it is mostly due to the assumed distance to the object. Nevertheless, this estimation is not unrealistic when compared with the expected duration of this phase ($t_{\text{sw}} 10^3\text{--}10^4$ yr, Kauff et al. 1993).

If a binary is involved in the shaping of the nebula, a common envelope evolution could provide enough rotation to start a dynamo effect. This dynamo would be able to produce an explosive outflow from which ansae could be created (Nordhaus & Blackman 2006; Nordhaus et al. 2007). Considering this, Nordhaus & Blackman (2006) derived a burst time of ~ 100 yr for the ansae in the planetary nebula NGC 7009. This time seems short when is compared with the 600 yr that we calculated in the shells of Frosty Leo. However, since Frosty Leo is a younger object and its distance is somewhat uncertain, it might be worth it to investigate if a dynamo could have produced the ansae with further modelling.

A computational model that could fit better with our results was proposed by Steffen, López & Lim (2001). The so-called stagnation knots model requires a time-dependent jet that drives into a CSE

forming knot-like structures (shells). At some point, the stream of material will stop and the shell slows down as it expands and continues adding mass from the envelope. This model can reproduce morphologies and speeds (240 km s⁻¹) similar to those we inferred in the NS and SS for an assumed distance of 3 kpc (see model b from Steffen et al. 2001), although, the time required to form shells is a bit larger (~ 1100 yr) than our 600 yr calculation. However, if we regard that our estimation is a lower limit, both ages are still comparable.

4.2 The polarization of the extended envelope in Frosty Leo

The EE in Frosty Leo and its geometry are seen in *J* and *H* bands (Figs 1 and 2). The largest angular size of the faint emission was detected in the *H* band where it shows a diameter of 35 arcsec. This EE can be understood as the remains of the previous AGB phase ejecta. Since the halo's shape seems spherical, the mass-loss in the first stages was probably isotropic. The polarization from *J* and *H* bands did not reveal new structures or trends. Nevertheless, the most noteworthy feature is the well-defined alignment from most of its polarization vectors (79° and 74°, in *J* and *H* bands, respectively).

Gledhill (2005) proposed that the vector alignment is caused by an optically thick media, under this assumption, most of the material in the nebula should concentrate at the equator in a dense disc. The disc is then responsible for the high optical depth and the alignment distribution. However, a high optical depth would have prevented us from detecting any structure in the bipolar regions, thus, this interpretation does not stand for the EE.

Since the EE (35 arcsec) is larger than the resolution of our data (1 arcsec), the PSF smoothing effect is also an unlikely answer (Piroola, Scaltriti & Coyne 1992; Gledhill 2005).

Whitney & Wolff (2002) showed that single scattering could also produce non-symmetric polarization, for this, the grains should be aligned by a magnetic field. In this model, a single source illuminating an optically thin cloud of non-spherical grains can account for some asymmetries in the polarization vector pattern. This could fit with our observational results assuming that the EE is illuminated directly by the star but the grains need to be coherently aligned by a strong magnetic field. Observations of OH Zeeman splitting and submillimetre polarimetry have shown magnetic fields of the order of mG in post-AGB stars (Bains et al. 2003; Sabin, Zijlstra & Greaves 2007). However, for this object, more observational evidence is required.

Multiple scattering is another alternative. This could occur when an envelope is not directly illuminated by the star, but by the light that has been already scattered. Previously scattered light reaching the envelope, could be scattered again by the material within and this results in an aligned polarization pattern (Bastien & Menard 1988; Fischer, Henning & Yorke 1994; Scarrott & Scarrott 1995; Wolf, Voshchinnikov & Henning 2002). A scenario where multiple scattering could account for our observational results is the following: the bipolar lobes are directly illuminated by the central star and scatter the light as a first event. Then, this light later reaches the EE and following scattering events could occur and result in the aligned polarization pattern. This scenario is quite similar to that proposed by Bastien & Menard (1988), only in their case, the subsequent scattering events occur in a circumstellar disc.

We favour an interpretation in which the EE is illuminated by scattered light coming from the lobes. This is the more likely physical situation for the EE, since the scattering dominates in the NIR (Scarrott et al. 1991; Bains et al. 2003).

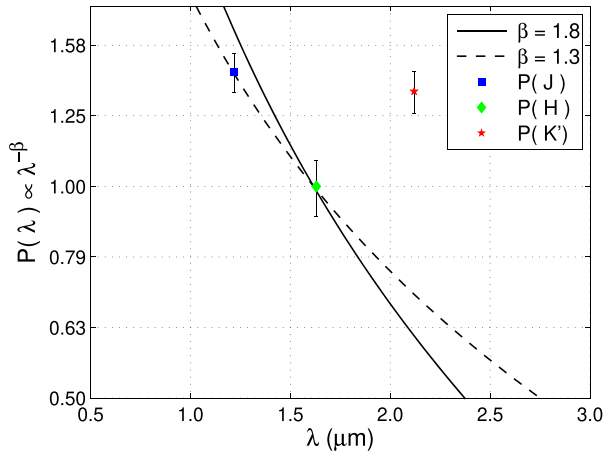


Figure 5. Average normalized polarization for the ES in J (square), H (diamond), and K' (star) bands. A decreasing tendency between J and H bands is observed, an index of $\beta = 1.3$ (dashed line) is needed to fit a $P(\lambda)$ power law. The ISM power law with an index $\beta = 1.8$ is also plotted for comparison (solid line). The K' -band polarization does not follow the power law, this is probably because it belongs to a deeper region (see the text in Section 4.3) and is plotted only to complete the NIR set of data.

4.3 Magnetic field nearby the central star of Frosty Leo?

The polarization maps from Murakawa et al. (2008) show a spot of aligned vectors located at the equator in both, H and K bands. The suggested mechanism of polarization in this area was the dichroism. A dichroic interpretation (directional extinction) requires aligned non-spherical grains. Such grains should tend to rotate with their longer axes orientated perpendicularly to the angular momentum vector. If a magnetic field is imposing the alignment, its direction should coincide with the angular momentum of the grains, thus, the transmitted electric vector (the polarization) is parallel to the mean-field direction (Whitney & Wolff 2002; Lazarian 2007; Crutcher 2012). Although our resolution is poorer (1 arcsec), our data in J , H , and K' bands also exhibit constant position angles in the same area (the ES, see Figs 3 and 4). According to Li & Greenberg (1997) and Martin et al. (1992), the dichroic interstellar medium (ISM) polarization at NIR wavelengths should follow the power-law $P(\lambda) \propto \lambda^{-\beta}$, where $\beta = 1.8 \pm 0.2$. This equation indicates that the polarization must follow a decreasing trend from shorter to larger wavelengths. Therefore, if the NIR polarization of an object follows this trend, it might belong to the dichroic case. If the coherent polarization seen in the ES is dichroic, this would indicate the presence of aligned grains and possibly, an ordering magnetic field with an orientation parallel to the equator. Otherwise, the multiple scattering plane proposed by Bastien & Menard (1988) would be a more suitable solution.

We investigated if the polarization in Frosty Leo follow the $P(\lambda)$ power law. To do so, we computed the average P per cent in the ES for each band and then compared them with the $P(\lambda)$ power law for several values of β . We found a decreasing tendency in the average polarization between J and H bands (see Table 2 and Fig. 5), but the index required to make a fit is $\beta = 1.3$ which is smaller than the predicted by Li & Greenberg (1997) and Martin et al. (1992). The P per cent goes up in the K' band, also moving away from the curve of theoretical polarization.

Although not entirely conclusive, these results compel us to reconsider the dichroic interpretation in the ES. However, there still are some arguments that should be taken into account before

discarding this possibility. For example, the increase in K' -band polarization could be explained by assuming that our map is probing deeper regions than J and H . The K -band data from Dougados et al. (1990) also supports this idea. If the light in our K' image is coming from a different layer, the polarization in this band might not be related to that in J and H or, caused by some other mechanism. Thus, the aligned and decreasing P per cent between J and H bands, could still be a hint of a dichroic effect occurring in the outer layers. Furthermore, recent submillimetre polarization studies of this source (Sabin et al. 2019) also suggest the presence of a magnetic field located at the equatorial region. The detection is marginal but the orientation of the inferred field would be parallel to the equator, just as the polarization in the NIR data suggests (Murakawa et al. 2008 and our own data), so we should not hurry in dismissing this idea. Further polarization investigations at far-IR and millimetre wavelengths could help obtaining more insights into this subject.

5 CONCLUSIONS

We studied the PPN Frosty Leo at NIR wavelengths using polarimetry and we detected the following features:

- (i) The NS and SS are seen in polarized emission. These shells are located at the tips of the bipolar nebula. Their centrosymmetric vector pattern indicate that the light is being scattered. They are clearly seen in J and H bands and cover large areas, in the K' band they are visible but less extended although this is probably due to our detection limit. We propose that these shells might be the remains of a fast ejection of material during a superwind event. The estimated duration is of 600 yr.
- (ii) The EE which is seen in polarized light and total intensity. This halo seen in J and H bands, has a diameter of 35 arcsec (in H band) and is the remaining material of the previous AGB phase. The PAs of the vectors associated to the EE indicate an alignment in J and H bands and are almost parallel to the equatorial plane of the nebula. This behaviour could be associated to multiple scattering since the light that reaches the EE is most likely coming from the bipolar lobes. Then, the material in the EE is probably scattering the light again into our line of sight resulting in the observed polarization.
- (iii) We performed a test to determine if the polarization in the equatorial region is due to aligned grains. We found a decreasing polarization between J and H bands, but, it is not consistent to match the $P(\lambda)$ power law for the ISM. Further polarization research at larger wavelengths are needed to solve this issue.

ACKNOWLEDGEMENTS

We thank the anonymous referee for the valuable comments that helped to improve the quality of this paper, and to all the personnel from the OAGH for the valuable help they provided during the observations. Thanks to Consejo Nacional de Ciencia y Tecnología, CONACYT-México for the fundings assigned to the project CB A1S54450 and the PhD scholarship with CVU 480840 to carry out this research. RD acknowledges to CONACYT-México for SNI grant (CVU 555629) and support from the European Research Council advanced grant H2020-ERC-2016-ADG-74302 under the European Union's Horizon 2020 Research and Innovation programme. This research made use of APLPY, an open-source plotting package for PYTHON (Robitaille and Bressert 2012). This publication makes use of data products from the Two Micron All Sky Survey, which is a joint project of the University of Massachusetts

and the Infrared Processing and Analysis Center/California Institute of Technology, funded by the National Aeronautics and Space Administration and the National Science Foundation. Some of the data presented in this paper were obtained from the Mikulski Archive for Space Telescopes (MAST). STScI is operated by the Association of Universities for Research in Astronomy, Inc., under NASA contract NAS5-26555.

REFERENCES

- Ageorges N., Walsh J., 2000, *A&A*, 357, 661
 Aller L. H., 1941, *ApJ*, 93, 236
 Bains I., Gledhill T., Yates J., Richards A., 2003, *MNRAS*, 338, 287
 Balick B., Frank A., 2002, *ARA&A*, 40, 439
 Bastien P., Menard F., 1988, *ApJ*, 326, 334
 Bujarrabal V., 1999, in Le Bertre T., Lebre A., Waelkens C., eds, *AGB circumstellar envelopes: molecular observations*, Proc. IAU Symp., Vol. 191. Cambridge Univ. Press, Cambridge, p. 363
 Bujarrabal V., Castro-Carrizo A., Alcolea J., Contreras C. S., 2001, *A&A*, 377, 868
 Carrasco L. et al., 2017, *Rev. Mex. Astron. Astrofís.*, 53, 497
 Clemens D. P., Leach R. W., 1987, *Opt. Eng.*, 26, 923
 Crutcher R. M., 2012, *ARA&A*, 50, 29
 Devaraj R., Luna A., Carrasco L., Vázquez-Rodríguez M., Mayya Y., Tánori J., Bernal E. S., 2018a, *PASP*, 130, 055002
 Devaraj R., Mayya Y., Carrasco L., Luna A., 2018b, *PASP*, 130, 055001
 Dougados C., Rouan D., Lacombe F., Forveille T., Tiphene D., 1990, *A&A*, 227, 437
 Fischer O., Henning T., Yorke H. W., 1994, *A&A*, 284, 187
 Forveille T., Morris M., Omont A., Likkell L., 1987, *A&A*, 176, L13
 Gledhill T., 2005, *MNRAS*, 356, 883
 Gledhill T., Chrysostomou A., Hough J., Yates J., 2001, *MNRAS*, 322, 321
 Hodapp K.-W., Sellgren K., Nagata T., 1988, *ApJ*, 326, L61
 Jones D., Boffin H. M., 2017, *Nat. Astron.*, 1, 0117
 Kauf H. U., Renzini A., Stanghellini L., 1993, *ApJ*, 410, 251
 Kwok S., 1993, *ARA&A*, 31, 63
 Lagadec E., 2016, in Liu X., Stanghellini L., Karakas A., eds, *Post-AGB nebular studies*, Proc. IAU Symp., Vol. 12. Cambridge University Press, Cambridge, p. 20
 Lazarian A., 2003, *J. Quant. Spectrosc. Radiat. Transfer*, 79, 881
 Lazarian A., 2007, *J. Quant. Spectrosc. Radiat. Transfer*, 106, 225
 Li A., Greenberg J. M., 1997, *A&A*, 323, 566
 Loup C., Forveille T., Omont A., Paul J., 1993, *A&AS*, 99, 291
 Martin P. et al., 1992, *ApJ*, 392, 691
 Maun N., Le Borgne J.-F., Picquette M., 1989, *A&A*, 218, 213
 Meixner M., Skinner C., Graham J., Keto E., Jernigan J., Arens J., 1997, *ApJ*, 482, 897
 Murakawa K., Ohnaka K., Driebe T., Hofmann K.-H., Oya S., Schertl D., Weigelt G., 2008, *A&A*, 489, 195
 Nordhaus J., Blackman E., 2006, *MNRAS*, 370, 2004
 Nordhaus J., Blackman E., Frank A., 2007, *MNRAS*, 376, 599
 Patriarchi P., Perinotto M., 1991, *A&AS*, 91, 325
 Piirola V., Scaltriti F., Coyne G., 1992, *Nature*, 359, 399
 Redman M., O'Connor J., Holloway A., Bryce M., Meaburn J., 2000, *MNRAS*, 312, L23
 Robinson G., Smith R., Hyland A., 1992, *MNRAS*, 256, 437
 Robitaille T., Bressert E., 2012, *Astrophysics Source Code Library*, record ascl:1208.017
 Roddier F., Roddier C., Graves J., Northcott M., 1995, *ApJ*, 443, 249
 Rounan D., Omont A., Lacombe F., Forveille T., 1988, *A&A*, 189, L3
 Sabin L., Zijlstra A. A., Greaves J., 2007, *MNRAS*, 376, 378
 Sabin L., Zhang Q., Vázquez R., Steffen W., 2019, *MNRAS*, 484, 2966
 Sahai R., Patel N., 2015, *ApJ*, 810, L8
 Sahai R., Bujarrabal V., Zijlstra A., 2000, *A&A*, 360, L9
 Scarrott S., Scarrott R., 1994, *MNRAS*, 268, 615
 Scarrott S., Scarrott R., 1995, *MNRAS*, 277, 277
 Scarrott S., Rolph C., Wolstencroft R., Tadhunter C., 1991, *MNRAS*, 249, 16P
 Skrutskie M. F. et al., 2006, *AJ*, 131, 1163
 Soker N., Rappaport S., 2000, *ApJ*, 538, 241
 Steffen W., López J. A., Lim A., 2001, *ApJ*, 556, 823
 Whitney B. A., Wolff M. J., 2002, *ApJ*, 574, 205
 Whittet D., 2004, in Witt A. N., Clayton G. C., Draine B. T., eds, *Astrophysics of Dust*, ASP Conf. Ser., Vol. 309, Proc. conf. held 26-30 May, 2003 in Estes Park, Colorado, p. 65
 Wolf S., Voshchinnikov N., Henning T., 2002, *A&A*, 385, 365
 Wolstencroft R., Scarrott S., Warren-Smith R., Walker H., Reipurth B., Savage A., 1986, *MNRAS*, 218, 1P

This paper has been typeset from a \TeX/L\TeX file prepared by the author.